Electronic Appendix 1: Supplementary text to accompany the manuscript, "Mantle melting as a function of water content beneath the Mariana arc."

Mariana Arc Whole Rock Data, Melt Inclusion Data and Primary Melt Compositions

Whole-rock major and trace element data for the host scoria samples used for melt inclusion work in this study are presented in Electronic Appendix 2. Major and trace elements for samples AGR19 and GUG-79-1 were analyzed by using the JY Ultima C ICP-AES and VG PQ ExCell ICP-MS at Boston University, following methods outlined by Kelley *et al.* (2003). Select major elements for samples AGR-Kimi, PB14, PB62 and PB64, in addition to trace elements, we analyzed using the Thermo X-Series II ICP-MS at the Graduate School of Oceanography, University of Rhode Island, also following techniques outlined by Kelley *et al.* (2003). Major and trace elements for sample SA93 are from the study of Meijer & Reagan (1981).

The complete data set for olivine-hosted melt inclusions from the Mariana arc is presented in Electronic Appendix 3. See the main text for analytical details.

Electronic Appendix 4 presents the modeled primary melt compositions for the least-fractionated, undegassed melt inclusions (see main text for screening criteria and reconstruction method), in addition to modeled pressures and temperatures of equilibration calculated using the thermobarometer of Lee *et al.* (2009). Averages for each island are given, and are also reported in the main text in Table 2.

Mariana Trough Data and Correction Scheme to Reconstruct Primary Melts

Figure A1 shows examples of liquid lines of descent preserved in glasses from the Mariana trough back-arc basin (see main text for data references). In order to accurately capture and correct for variations in LLD's due to variations in H_2O, the data have been split into three groups by H_2O content: <1 wt.%, 1.0-1.5 wt.%, and >1.5 wt.% H_2O. The point of plagioclase-in was chosen either by visible kink in the LLD (>1.5 wt.% group; 7.1 wt.% MgO), the most MgO-rich sample in the group (1.0-1.5 wt.% group; 7.4 wt.% MgO), or by analogy with MORB (<1 wt.% group; 8.5 wt.% MgO). Ol+plag±cpx crystallization trends were determined empirically using linear regression of data in each group with MgO<MgO @ plag-in. Electronic Appendix 5 presents the average slopes used to correct each data point back to the composition at plag-in.

Sensitivity Test of Batch Model Results to Uncertainties in Individual Variables

The method used to invert melt composition for melt fraction (F) and concentration of H_2O in the mantle source ($C^o_{H_2O}$) is sensitive to errors and uncertainties in model inputs. Here we present a sensitivity test of model results for a subset of data to isolated variables in the inversion model.

• Forsterite content of mantle olivine

The method presented in the main text references all reconstructed primary melt compositions to equilibrium with mantle olivine at Fo_{90}. If the residual mantle is more fertile, the Fo content of residual olivine could be lower (e.g., Fo_{89}), or if it is left significantly depleted by high extents of melting, the Fo content of the residual olivine may be higher (e.g., Fo_{91}). Figure A2 shows the sensitivity of model results to different

reference Fo contents, ranging from Fo_{89} to Fo_{91}. Differences in model results between Fo_{89} and Fo_{90} are small, yielding differences of 0 to 1% (absolute) in calculated F, and 0-0.01 wt.% (absolute) in $C^o_{H_2O}$. Differences in model results between Fo_{90} and Fo_{91} are slightly greater, yielding differences of 0 to 2% (absolute) in calculated F, and 0-0.01 wt.% (absolute) in $C^o_{H_2O}$. The net effect of this variable on data arrays is a slight horizontal translation of 0-2% F (absolute).

• Concentration of TiO_2 in the Mariana Arc Mantle Source

Uncertainties in the absolute value of $C^o_{TiO_2}$ applied for the Mariana arc (0.123 wt.% TiO_2; see main text) and in the assumption of constant $C^o_{TiO_2}$ among the four arc volcanoes may have significant impact on the modeling results. Figure A3a shows the sensitivity of model results to ±10% variations in $C^o_{TiO_2}$ (from 0.111 to 0.135 wt.% TiO_2), assuming a constant source beneath all volcanoes. Errors in F and $C^o_{H_2O}$ due to uncertainties in $C^o_{TiO_2}$ are highly correlated on Figure A3a, showing differences of ±1-3% F (absolute) and ±0.03-0.10 wt.% $C^o_{H_2O}$ (absolute). Figure A3b shows the sensitivity of model results to volcano-specific variations in $C^o_{TiO_2}$, which are constrained here using the TiO_2/Y model outlined in the main text. The four islands are within ±10% of each other in $C^o_{TiO_2}$ calculated using this model, with Guguan and Agrigan nearly identical to the average used for the whole arc (0.125 wt.% $C^o_{TiO_2}$), Sarigan more depleted (0.110 wt.% $C^o_{TiO_2}$), and Pagan more enriched (0.135 wt.% $C^o_{TiO_2}$). The net effect of this variable is movement of model points in or out of the origin on Figure A3, yielding a small influence on the slopes/shapes of data trends, but significant differences in the absolute

values of F or $C^o_{H_2O}$. Allowing the mantle source to vary with each volcano would create slightly more spread among the data arrays for each island, distinguishing Pagan and Sarigan more clearly from Agrigan and Guguan.

• Mantle-Melt Partition Coefficients for H_2O and TiO_2

Uncertainties in the absolute values of mantle/melt partition coefficients D_{H2O} and D_{TiO2} and in the assumption of constant D_{H2O} and D_{TiO2} over a large range of residual peridotite compositions may also have significant impact on the modeling results. Partition coefficients have been shown to decrease by ~50% from relatively fertile to depleted peridotite (McDade *et al.*, 2003), and sensitivity of the model results to such variations is thus important to constrain. Recent determinations of D_{H2O} have yielded smaller values than the D_{H2O} used by this study (0.012, this study; 0.009, Aubaud *et al.*, 2004; 0.007, Hauri *et al.*, 2006). Figure A4 shows the sensitivity of model results to variations in D_{H2O} at the lowest determined value of 0.007. Differences in model results even over this large variation in D_{H2O} are practically indistinguishable (0.01-0.02 wt.% $C^o_{H_2O}$, absolute). This outcome shows that the model results are essentially insensitive to the value used for D_{H2O}, within ±50%, justifying both the value of D_{H2O} used and the assumption of constant D_{H2O}. The model results are more sensitive to the value of D_{TiO2} used. Figure A5a shows the impact of ±25% variation in D_{TiO2} (0.03 to 0.05), assumed constant among all samples. As with $C^o_{TiO_2}$, errors resulting from uncertainty in D_{TiO2} are correlated, causing model points to move in or out of the origin, and giving differences of ±1% F (absolute) and ±0.02-0.05 wt.% $C^o_{H_2O}$ (absolute). Figure A5b shows the result of a simple model allowing D_{TiO2} to decrease by 50% as F increases from 10% to 22%. The

values applied for D_{TiO2} were 0.04 for F≤10%, 0.03 for 10%<F<15%, and 0.02 for F≥15%. In all cases, the net effect of allowing D_{TiO2} to vary with F on data trends from each island would be a slight shallowing of the slopes on Figure A5.

Monte Carlo Error Analysis of Batch Melting Model

Here we present a comprehensive Monte Carlo random error analysis on the variables input to the batch melting inversion, to show the combined effects of uncertainties and errors on the model output. The error analysis incorporates uncertainties of ±5% in the raw concentrations of TiO_2 and H_2O in the melt inclusions (assumed to be analytical error), ±25% in the amount of olivine added back to reach Fo_{90} (equivalent to the difference between Fo_{89} and Fo_{91}, as explored above), ±10% in $C^o_{TiO_2}$ as explored above, and ±25% in D_{TiO2} and D_{H2O} as explored above. A Monte Carlo simulation of the batch model was run through 1000 iterations, allowing for random variation of each variable within the set boundaries of uncertainty. The 900 intermediate solutions were used to generate error ellipses (90% confidence) around the modeled data points presented in the main text of this work, which are shown on Figure A6. Within each island, the error ellipses for the selected points do not overlap within error, indicating that the model points within the data arrays from each island are statistically distinguishable.

Figure Captions

Figure A1. Liquid lines of descent for Mariana trough basalts. Symbols are colored to indicate water content groups 0-1.0 wt.% H_2O (red), 1.0-1.5 wt.% H_2O (brown), and >1.5 wt.% H_2O (blue). Darker blue symbols within this group have MgO greater than MgO at

plagioclase-in. (a) Al_2O_3 vs. MgO, with least-squares linear regressions through data points withn each group with MgO<MgO at plag-in. (b) FeO* vs. MgO, where FeO* is total Fe reported as FeO, with least-squares linear regressions through data points within each group with MgO<MgO at plag-in. See Electronic Appendix 5 for average slopes for all the major elements, used to correct fractionated Mariana trough basalts back to MgO at plag-in.

Figure A2. Plot of $C^o_{H_2O}$ vs. melt fraction (*F*), showing the effect on select model points of referencing reconstructed primary melts to different values of the forsterite content of mantle olivine. Each point is labeled with the Fo content of the reference olivine used, larger symbols are the model points presented in the main text of the paper, referenced to Fo_{90}.

Figure A3. Plots of $C^o_{H_2O}$ vs. melt fraction (*F*), showing (a) the effect on select model points of ±10% variations in $C^o_{TiO_2}$ and (b) the effect of volcano-specific variations in $C^o_{TiO_2}$. Each point is labeled with the value of $C^o_{TiO_2}$ used. Larger symbols between labeled points are the model points presented in the main text of the paper, using $C^o_{TiO_2}$=0.123.

Figure A4. Plot of $C^o_{H_2O}$ vs. melt fraction (*F*), showing the effect on select model points of varying D_{H2O}. Each point is labeled with the D_{H2O} used, larger symbols are the model points presented in the main text of the paper, using D_{H2O}=0.012.

Figure A5. Plots of $C^{o}_{H_2O}$ vs. melt fraction (F), showing (a) the effect on select model points of ±25% variations in D_{TiO2} and (b) the effect of a simple model allowing D_{TiO2} to decrease with increasing F. Each point is labeled with the value of D_{TiO2} used. Larger symbols are the model points presented in the main text of the paper, using D_{TiO2}=0.04.

Figure A6. Plot of $C^{o}_{H_2O}$ vs. melt fraction (F), showing the effect on select model points of combined random uncertainties in model input variables, using a Monte Carlo simulation. Solid filled symbols are the model points presented in the main text of the paper. Shaded ellipses surrounding each model point show the errors associated with each model point (90% confidence).

References

Aubaud, C., Hauri, E. H. & Hirschmann, M. M. (2004). Hydrogen partition coefficients between nominally anhydrous minerals and basaltic melts. *Geophysical Research Letters* 31.

Hauri, E. H., Gaetani, G. A. & Green, T. H. (2006). Partitioning of water during melting of the Earth's upper mantle at H2O-undersaturated conditions. *Earth and Planetary Science Letters* 248, 715-734.

Kelley, K. A., Plank, T., Ludden, J. N. & Staudigel, H. (2003). Composition of altered oceanic crust at ODP Sites 801 and 1149. *Geochemistry Geophysics Geosystems* 4, doi:10.1029/2002GC000435.

Lee, C.-T. A., Luffi, P., Plank, T., Dalton, H. & Leeman, W. P. (2009). Constraints on the depths and temperatures of basaltic magma generation on Earth and other terrestrial planets using new thermobarometers for ma. *Earth and Planetary Science Letters* 279, 20-33.

McDade, P., Blundy, J. D. & Wood, B. J. (2003). Trace element partitioning between mantle wedge peridotite and hydrous MgO-rich melt. *American Mineralogist* 88, 1825-1831.

Meijer, A. & Reagan, M. K. (1981). Petrology and geocehmistry of the island of Sarigan in the Mariana arc: Calc-alkaline volcanism in an oceanic setting *Contributions to Mineralogy and Petrology* 77, 337-354.

Figure A1

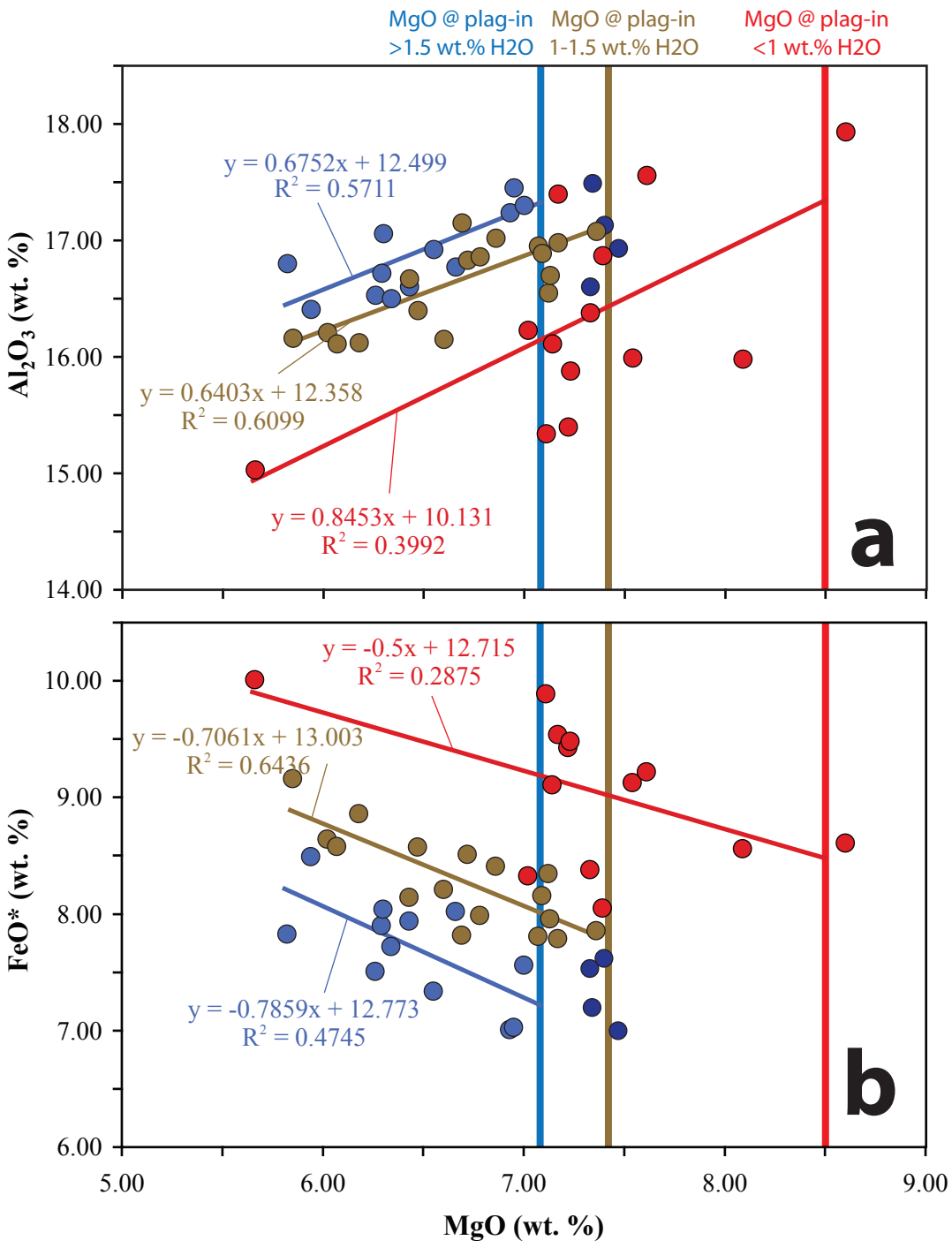
MgO @ plag-in
>1.5 wt.% H2O
MgO @ plag-in
1-1.5 wt.% H2O
MgO @ plag-in
<1 wt.% H2O
y = 0.6752x + 12.499
R2 = 0.5711
y = 0.6403x + 12.358
R2 = 0.6099
y = 0.8453x + 10.131
R2 = 0.3992
a
y = -0.5x + 12.715
R2 = 0.2875
y = -0.7061x + 13.003
R2 = 0.6436
y = -0.7859x + 12.773
R2 = 0.4745
b
Al2O3 (wt. %)
FeO* (wt. %)
MgO (wt. %)
18.00
17.00
16.00
15.00
14.00
10.00
9.00
8.00
7.00
6.00
5.00
6.00
7.00
8.00
9.00

Figure A2

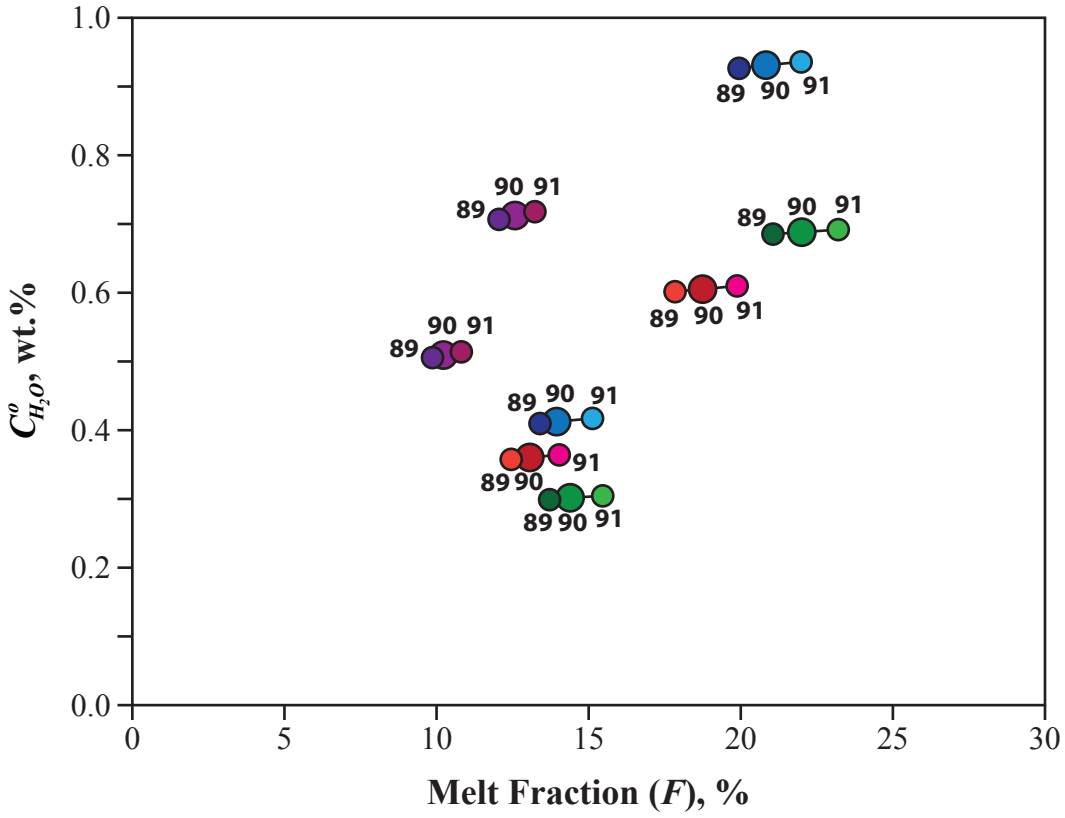
1.0
0.8
0.6
0.4
0.2
0.0
0
5
10
15
20
25
30
$C^o_{H_2O}$, wt.%
Melt Fraction (*F*), %
89 90 91
89 90 91
89 90 91
89 90 91
89 90 91
89 90 91
89 90 91
89 90 91

Figure A3

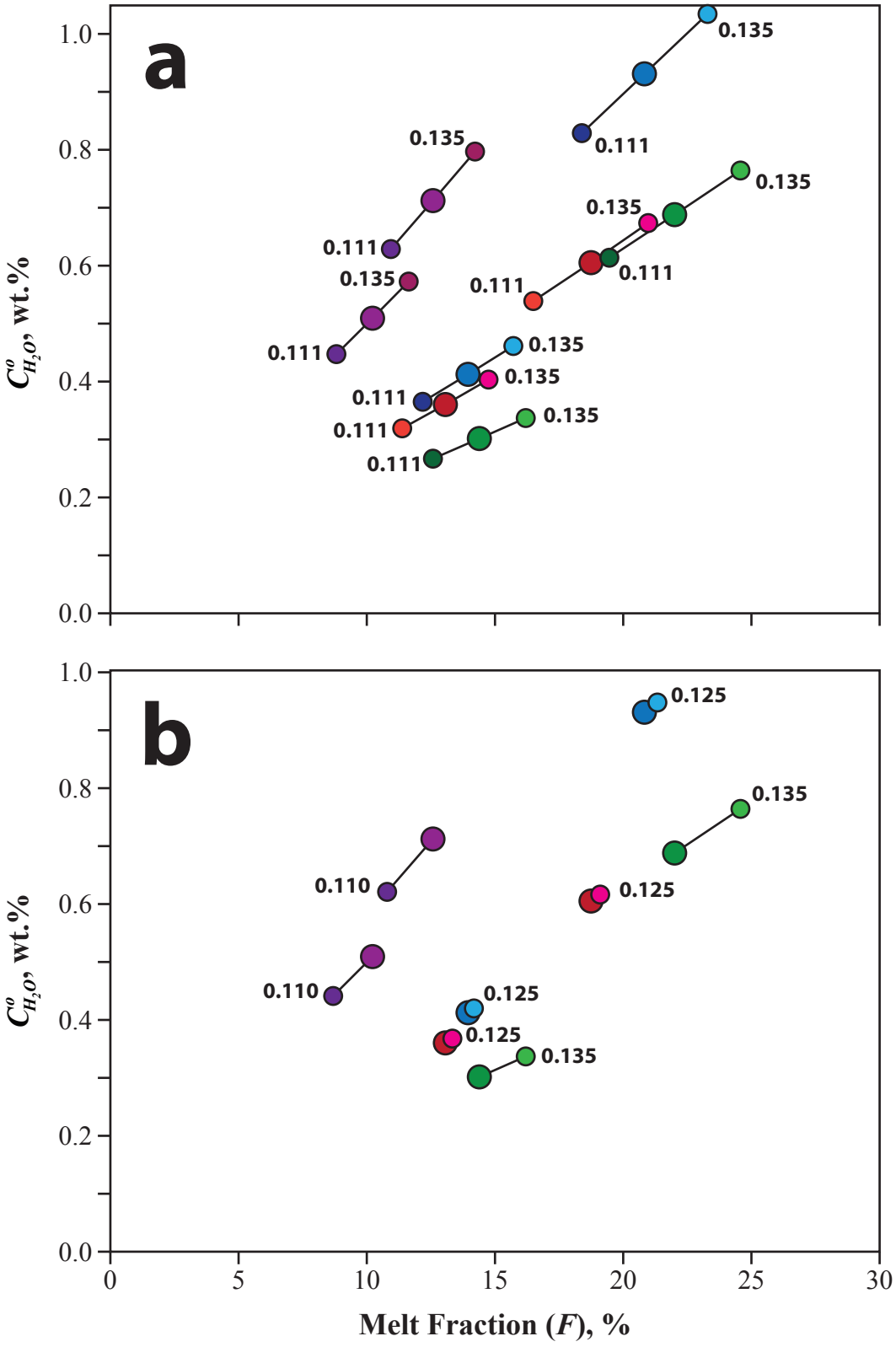

Figure A4

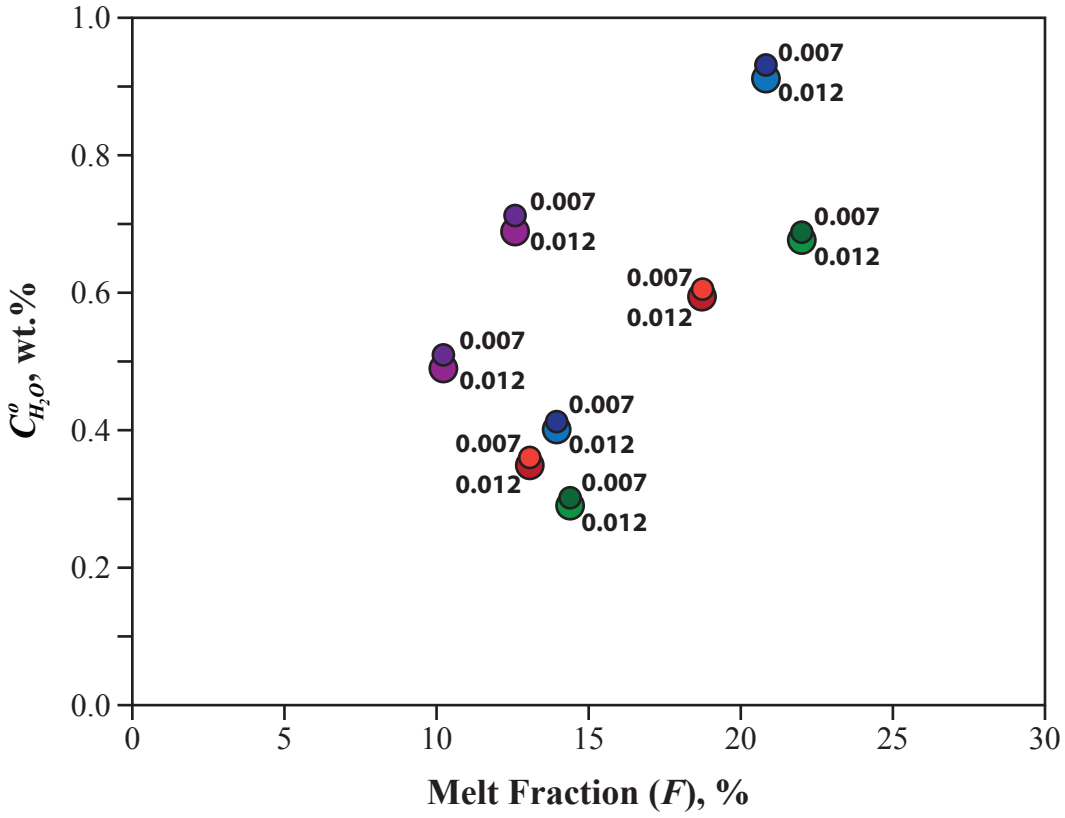
1.0
0.8
0.6
0.4
0.2
0.0
0
5
10
15
20
25
30
$C^o_{H_2O}$, wt.%
Melt Fraction (*F*), %
0.007
0.012
0.007
0.012
0.007
0.012
0.007
0.012
0.007
0.012
0.007
0.012
0.007
0.012
0.007
0.012

Figure A5

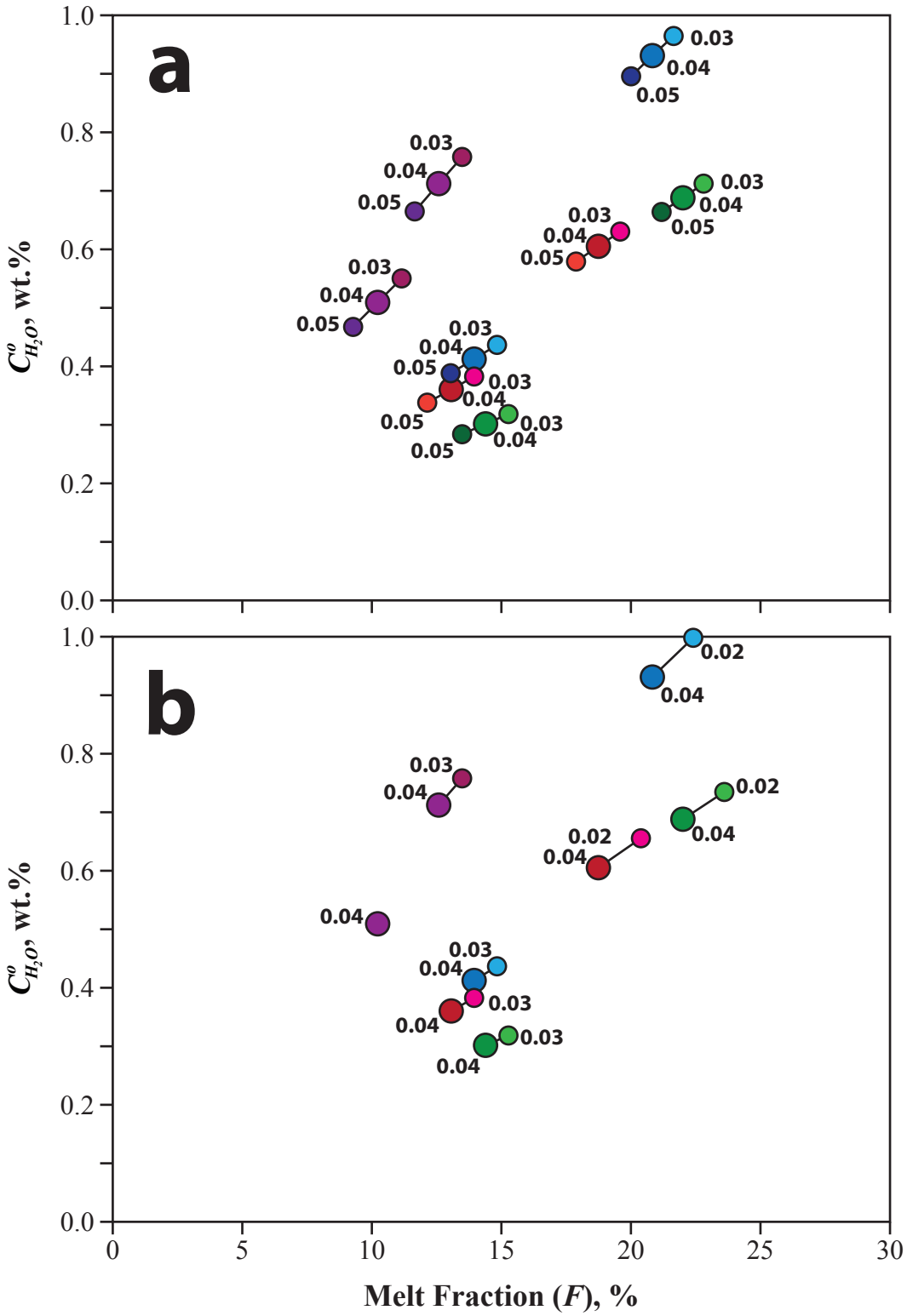
a
b
$C^o_{H_2O}$, wt.%
Melt Fraction (F), %
0.0
0.2
0.4
0.6
0.8
1.0
0
5
10
15
20
25
30
0.02
0.03
0.04
0.05

Figure A6

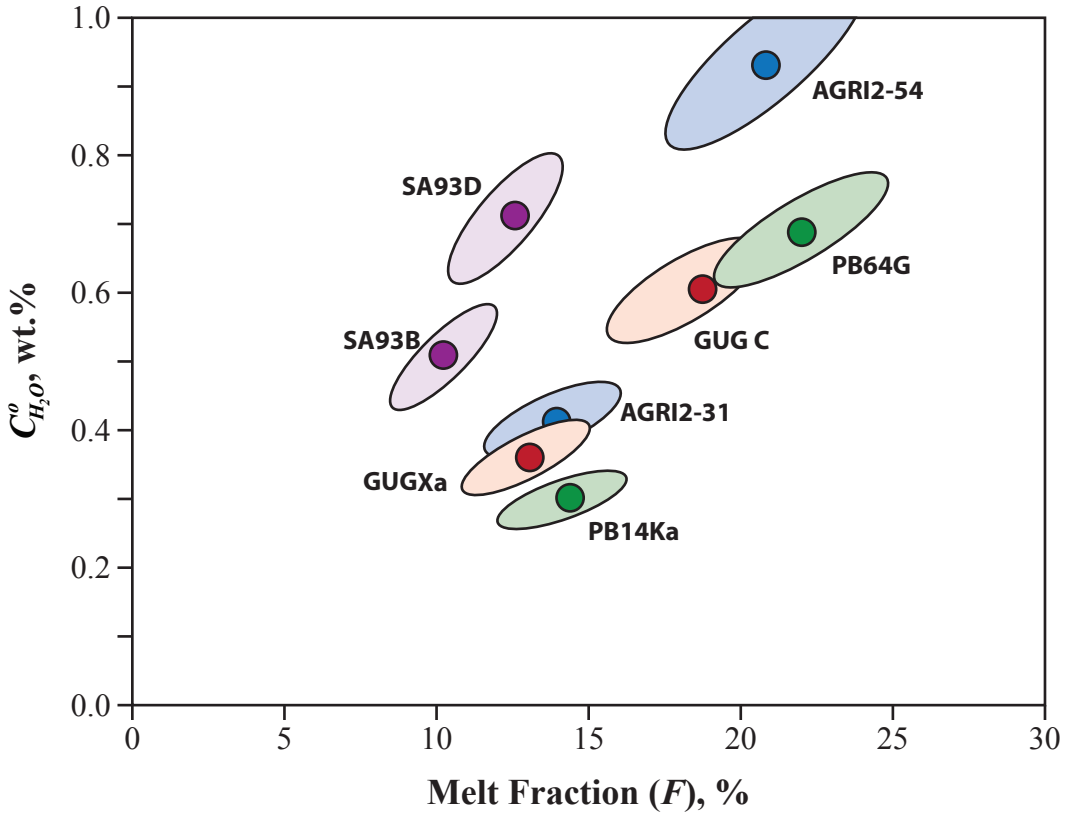
1.0
0.8
0.6
0.4
0.2
0.0
0
5
10
15
20
25
30
$C^o_{H_2O}$, wt.%
Melt Fraction (*F*), %
AGRI2-54
SA93D
PB64G
SA93B
GUG C
AGRI2-31
GUGXa
PB14Ka